Localized Corrosion of Corrosion Resistant Alloys in H_2S-Containing Environments

Liu Cao,[‡,] Andre Anderko,[**] Feng Gui,[*] and Narasi Sridhar[*]*

ABSTRACT

Corrosion resistant alloys (CRAs) are widely used in harsh oil and gas production environments where low-alloy steels cannot be used. It is recognized that stress corrosion cracking (SCC) of stainless steels and Ni-based alloys can occur at potentials above the repassivation potential (E_{rp}) for localized corrosion. This paper focuses on experimental work that has been conducted to determine E_{rp} of six CRAs, i.e., super-martensitic stainless steels S13Cr (UNS S41425) and S15Cr (UNS S42625), super-duplex stainless steel 2507 (UNS S32750), and solid solution Ni-based Alloys 2535 (UNS N08535), 29 (UNS N08029), and 28 (UNS N08028) in chloride-H_2S environments. A generalized approach is applied to determine E_{rp} values from electrochemical polarization results at temperatures ranging from 85°C to 232°C. The use of completely deaerated solutions and ensuring the stable growth of localized corrosion are both critical to obtain conservative E_{rp} values for CRAs in environments that are similar to downhole conditions. A part of the obtained data set has been used in the development of a mechanistic model for calculating E_{rp} as a function of alloy composition, environment chemistry, and temperature in order to generalize the observations and predict localized corrosion and SCC in a wide range of chloride-H_2S environments by using limited experimental tests. Another part of the E_{rp} data set has been used to validate the model predictions. It has been demonstrated that the model predictions agree well with the experimental E_{rp} values. Based on the measurements coupled with model predictions, the effects of H_2S, temperature, and alloying elements on the susceptibility of CRAs to localized corrosion and SCC are analyzed.

KEY WORDS: corrosion resistant alloys, high pressure and high temperature, hydrogen sulfide corrosion, localized corrosion, repassivation potential, stress corrosion cracking

INTRODUCTION

The oil and gas industry is moving into deeper waters and deeper reservoirs for drilling and production as a result of dwindling production from easily accessible shallow reservoirs. The new discoveries since the mid-80's and early 90's have been made in water depths greater than 1,500 m (4,900 ft).[1] Temperature and pressure in such deep reservoirs dramatically increase with the well depth. Pressures and temperatures approaching 160 MPa (23,000 psi) and 300°C, respectively, have been estimated for depths greater than 10,000 m (32,800 ft).[2-4] The environments in the high-pressure and high-temperature (HPHT) deep wells usually contain aggressive species, i.e., a mixture of H_2S and CO_2, coupled with extremely low oxygen fugacity. In addition to H_2S, extreme environments usually have concentrations of CO_2 greater than 3%.[5-6] Elemental sulfur (S^0) could be found if the concentration of H_2S is greater than 5% to 10%.[6-9] Finally, traces of mercury and organic acids (mostly acetic acid, HAc) are common in the gas phase of deep and ultra-deep wells.[7] The composition of the water will change with the life of the well. In a NACE survey,[5] a wide spectrum of chloride concentrations in produced waters is reported, ranging from 2,000 ppm to 200,000 ppm.

Submitted for publication: January 2, 2016. Revised and accepted: March 26, 2016. Preprint available online: January 27, 2016, http://dx.doi.org/10.5006/2016.

‡ Corresponding author. E-mail: liu.cao@dnvgl.com.
* DNV GL, 5777 Frantz Road, Dublin, OH 43017.
** OLI Systems, Inc., 240 Cedar Knolls Road, Suite 301, Cedar Knolls, NJ 07927.

ISSN 0010-9312 (print), 1938-159X (online)

As a result of the increasingly harsh environments in the HPHT deep wells, corrosion resistant alloys (CRAs) are often used for downhole tubulars and in other production equipment. Depending on the actual production conditions, the CRAs include martensitic stainless steels (SS), duplex stainless steels (DSS), nickel-based alloys, and nickel-cobalt alloys. The CRAs exhibit excellent resistance to general corrosion, which carbon steels lack. However, they suffer from localized corrosion and environmentally assisted cracking (EAC) in sour production environments. The frequently encountered EAC forms include, but are not limited to, sulfide stress cracking (SSC), hydrogen stress cracking (HSC), and stress corrosion cracking (SCC). The SSC and HSC are both driven by the formation of atomic hydrogen, either from the hydrogen ion reduction reaction (in H_2S environments) or as a result of galvanic coupling with carbon steel, respectively. These two hydrogen-induced cracking modes normally occur in sour environments at low temperatures and low pH (below depassivation pH) or under galvanic contact with carbon steel, where hydrogen generation and transport have a significant impact. In contrast, SCC is mainly controlled by the stability of the passive film and by the local chemistry, thus making it sensitive to the pH, temperature, redox potential, and the halide anion concentration, not only in the bulk solution but also in the occluded local environment. SCC can occur over wide ranges of conditions, including a wide span of pH (above depassivation pH) and at the moderate to high temperatures that are critical to downhole applications.

At present, the materials specifications of CRAs are scattered around in a combination of standard tests,[10] fit-for-purpose testing,[11] company specifications, guidance documents (e.g., EFC No. 17),[7] empirical knowledge-based standards (e.g., ISO 15156),[12-13] and operator experience. The environmental conditions in the standards for oil and gas production cover all three failure modes. For SCC, the boundaries of acceptable performance of CRAs are often specified in terms of chloride level, pH, temperature, and H_2S and CO_2 partial pressure based on empirical observations and some experimental data from the literature.[12-13] In fact, it is not known how much performance is affected when these limits are exceeded. Because there are other environmental factors that affect the field performance, the relationship between accelerated laboratory tests and the actual field application is often not quantified. Furthermore, the field environment may change over time as a result of a variety of factors; therefore, the performance of a specific material over the lifetime of a project is an important consideration.

It has been generally recognized that localized corrosion can be a precursor to SCC,[6,14-15] which is a result of similar critical local environment conditions that trigger the growth of pits/crevice corrosion and stress corrosion cracks. Thus, SCC can be initiated from localized corrosion sites and sustained to grow when the corrosion potential (E_{corr}) of an alloy exceeds the critical potential (i.e., the repassivation potential, E_{rp}), assuming that the local strain rate on the materials remains above a threshold value and E_{rp} is not significantly affected by plastic deformation in the initial stage of crack initiation. There is experimental evidence indicating that SCC occurs at potentials above the E_{rp} for localized corrosion and cracks grow at potentials more positive than E_{rp}.[16-17] It may be argued that for the lower grades of CRAs, SCC can occur in the potential region of the active-passive transition peak, as it does for carbon steel in aggressive environments. In fact, for this to happen, the pH value has to be slightly above the depassivation pH (pH_d) for the alloy to exhibit significant active-passive transition. If the pH is below pH_d, then fully active dissolution occurs, whereas if it is sufficiently above pH_d, then there is no significant active-passive transition peak. For many of the higher grades of CRAs, pH_d is quite low, around 1.[18]

Based on this assumption that localized corrosion is a driver for SCC, the onset of SCC can be described in a quantitative manner by using three parameters that quantify the traditional three qualitative factors for SCC, i.e., two electrochemical parameters and mechanical parameters, as indicated in Figure 1. The comparison of E_{rp} and E_{corr} can be used to evaluate the susceptibility to localized corrosion and SCC in a given environment. However, little work can be found in the literature on the determination of E_{rp} of CRAs in sour environments.[6,19] This is likely a result of the experimental challenges in performing electrochemical measurements in the presence of H_2S at HPHT conditions. Thus, it is of interest to develop a predictive approach to evaluate the performance of an alloy in a broad range of environments using a physical model based on a limited set of experimental data, which is capable of generalizing the experimental database and extrapolating from laboratory tests to field conditions. The development of a framework for modeling E_{rp} and E_{corr} as a function of alloy composition, environment chemistry, temperature, and

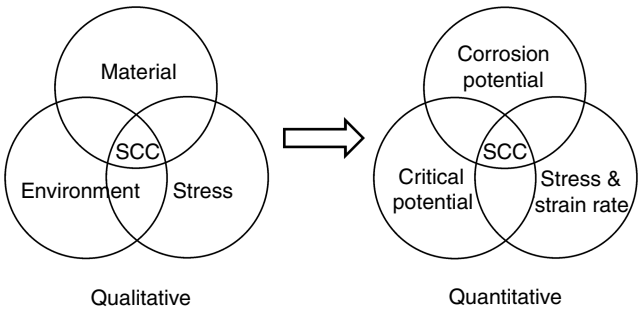

FIGURE 1. *Qualitative and quantitative deterministic factors for SCC initiation and propagation.*

TABLE 1
Compositions of the Alloys Studied (wt%)

Alloy	UNS No.	Ni	Fe	Cr	Mo	N	C	Other	PRE_N[(A)]
S13Cr	S41425	5.9	bal.	12.1	1.9	0	0.01		18
S15Cr	S42625	6.3	bal.	14.6	1.9	0	0.03	Cu 0.97, Mn 0.28, Si 0.36	21
2507	S32750	6.93	bal.	25.17	3.87	0.27	0.017	Cu 0.40, Mn 0.8, Si 0.28	42
2535	N08535	30.6	bal.	24.7	2.78	0	0.02	Cu 0.81, Mn 0.6, Si 0.29	34
29	N08029	31.5	bal.	27.0	4.4	0	≤0.02	Cu 1.0, Mn≤2.5, Si ≤1.0	42
28	N08028	31.0	bal.	27.0	3.5	0	≤0.02	Cu 1.0, Mn≤2.0, Si ≤0.6	39

(A) PRE_N, $F_{PREN} = Cr + 3.3(Mo + 0.5\ W) + 16N$, pitting resistance equivalent number is calculated by Equation (1) in ISO 15156 – part 3.

pressure will enable rationalizing and predicting localized corrosion and SCC of CRAs at oil and gas production conditions.

In previous studies,[20-22] a computational model for E_{rp} was developed and applied to chloride-H_2S systems. The model has been validated by using a recent comprehensive set of E_{rp} data for S13Cr SS (UNS S41425)[(1)] at 85°C. The model considers competitive adsorption of electrochemically active species, e.g., chloride and adsorbed sulfur, and competitive formation of metal oxide and sulfide in the process of repassivation. An interesting finding of an inhibitive effect of small amounts of H_2S on S13Cr SS in dilute chloride solutions was validated by the model, and also independently proven by the experimental work of Hinds, et al.[19] In this study, more details of the experimental work performed on S13Cr SS at 85°C are discussed and the method for determining E_{rp} of CRAs in H_2S-containing environments is generalized. New experimental measurements of E_{rp} of five other CRAs, i.e., S15Cr SS (UNS S42625), DSS 2507 (UNS S32750), Alloy 2535 (UNS N08535), Alloy 29 (UNS N08029), and Alloy 28 (UNS N08028) at 85°C and HPHT conditions are reported to extend and verify the model predictions. These measurements are intended to provide the crevice repassivation potential, which constitutes the lower bound of E_{rp} and is thus appropriate for a conservative prediction of localized corrosion. Furthermore, the corrosion behavior of the tested CRAs in sour environments are compared and discussed with regard to H_2S concentration, temperature, and alloying elements.

EXPERIMENTAL PROCEDURES

Materials and Specimens

Electrochemical tests were performed on selected CRAs that are used in oil and gas production, i.e., on two super-martensitic stainless steels (S13Cr SS and S15Cr SS), a super-duplex stainless steel (DSS 2507), and three solid-solution Ni-based alloys (Alloys 2535, 29, and 28). The CRA specimens were cut out from tubular materials and machined into various geometries. The chemical compositions of the CRAs are listed in Table 1. Both cylindrical coupons and prismatic crevice specimens were used for S13Cr SS in the electrochemical experiments, with the dimensions shown in Figure 2. Thereafter, only crevice specimens were used for the rest of CRAs, which generated conservative E_{rp} values. The sample surface was abraded to 600 grit by SiC sandpaper, then cleaned with isopropanol in ultrasonic bath, and finally dried by blowing nitrogen. As per ASTM Standard G192,[23] the creviced specimens were assembled using ceramic multiple-crevice formers wrapped in PTFE tape. Fasteners and washers were made of titanium alloy. Seventy in·lbf (7.91 N·m) torque was applied on the assembly to ensure the formation of critical crevice geometry for CRAs.

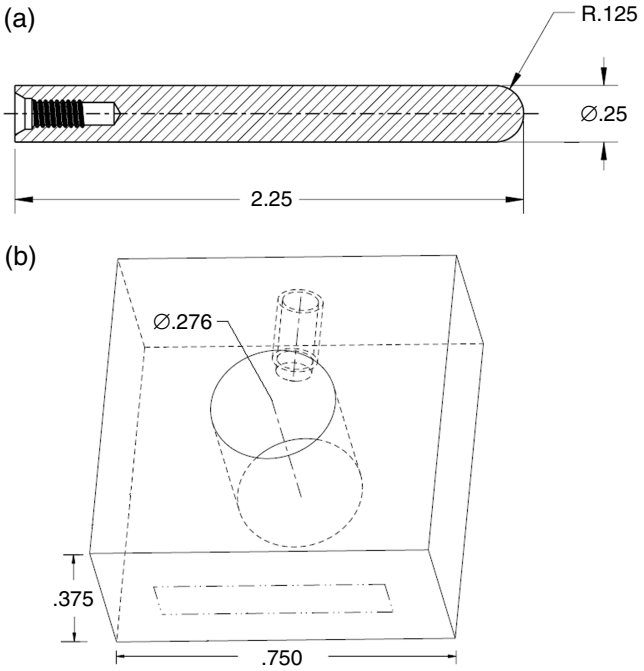

FIGURE 2. *Schematic drawings of (a) cylindrical coupon and (b) prismatic crevice specimen used in the electrochemical experiments for E_{rp} determination (unit: in).*

(1) UNS numbers are listed in *Metals and Alloys in the Unified Numbering System*, published by the Society of Automotive Engineers (SAE International) and cosponsored by ASTM International.

TABLE 2
Environment Conditions of Electrochemical Tests

Alloy	Temperature	Pressure[A]	Chloride (NaCl)	H_2S (wt%)[B]
S13Cr S15Cr[C]	85°C	ambient	0.0003 m 0.003 m 0.03 m 0.3 m 3.0 m	 0% (nitrogen) 1% 100%
2507	85°C	ambient	0.003 m 0.03 m 0.3 m 3.0 m	0% (nitrogen) 1% 100%
2535	85°C	ambient	2.5% 25%	0% (nitrogen) 100%
	232°C	~880 psig (6.1 MPa)	2.5% 25%	0% (nitrogen) 75%
29	85°C	ambient	1.65%[D] 25%	0% (nitrogen) 100%
28[C]	150°C	~400 psig (2.8 MPa)	1.65% 25%	0% (nitrogen) 100%
	200°C	~700 psig (4.8 MPa)	1.65% 25%	0% (nitrogen) 75%

[A] Total pressure at testing temperature.
[B] This was the gas phase composition at room temperature. Before heating up, 250 psig (1.7 MPa) pressurized vessel was used for tests at 150°C; 350 psig (2.4 MPa) pressurized vessel was used for tests at 200°C and 232°C.
[C] Only selected conditions were performed to spot-check model prediction.
[D] Equivalent to 10,000 ppm chloride concentration.

Experimental Conditions

Electrochemical experiments were performed in NaCl solutions with concentrations ranging from 3 molal (m) to 0.0003 m. All tests were performed at 85°C and ambient pressure with and without the presence of H_2S, as listed in Table 2. Different concentrations of H_2S gas mixtures (wt%, balanced with nitrogen) were used to investigate the H_2S effect. Higher temperature and pressure conditions were investigated only for the Ni-based alloys in a pressure vessel. In all tests, the solution and the testing cell/vessel were thoroughly deaerated with research grade nitrogen to rigorously remove dissolved oxygen, which is critical for electrochemical measurements on CRAs. In addition to the fact that downhole environments are mostly oxygen-free, the corrosion potential of CRAs is quite sensitive to the presence of oxidizing species, and dissolved H_2S can interact with dissolved oxygen to produce S^0. Only deaerated conditions allow investigating the complete anodic behavior in H_2S-containing environments. Nitrogen or H_2S gas mixtures were either purged through the cell during the experiments at ambient pressure, or charged in the pressure vessel at predetermined partial pressures before heating up the vessel to the testing temperature (>100°C).

Electrochemical Experiments

For super-martensitic and duplex stainless steel specimens, i.e., for S13Cr SS, S15Cr SS, and DSS 2507, electrochemical measurements were conducted in a traditional three-electrode glass cell as per ASTM Standard G5.[24] It consisted of a working electrode holder, a saturated calomel electrode (SCE) as the reference in a water-cooled Luggin probe (filled with test solution), and a platinized niobium (Pt/Nb) coil as the counter electrode, as illustrated in Figure 3(a). The electrochemical glass cell held approximately 800 mL of solution in all tests. The solution was first deaerated in the glass cell for at least 2 h at 85°C without the sample installed. Water vapor was collected by a tap water-cooled condenser and flowed back into the cell. The prepared sample was mounted on the working electrode holder as described in ASTM Standard G5,[24] and quickly installed in the glass cell while maintaining nitrogen purging (with a positive pressure inside the glass cell). The sample was kept hanging over the solution surface in the nitrogen blanket for 10 min to 15 min to remove any introduced oxygen. Then, it was lowered and either partially immersed in the case of the cylindrical coupons (to avoid crevice corrosion underneath the PTFE compression gasket of electrode holder) or fully immersed in the case of the crevice specimens. Open circuit potential (OCP) of the specimen was monitored overnight with research grade nitrogen sparging and subsequently for 2 h after introduction of H_2S gas mixture.

For the solid-solution Ni-based alloys specimens, i.e., Alloys 2535, 29, and 28, HPHT electrochemical measurements were conducted in a 250 mL multi-port testing vessel made of Alloy C276 (UNS N10276), as illustrated in Figure 3(b). Multiple threaded ports on the lid allow thermal well, electric wires, and gas tube to go through. A PTFE O-ring was used to seal between the lid and body when they were bolted together. Wires ran through Conax[†] sealing glands to hold high pressure. A Pt/Nb coil was used as a counter electrode, which was embedded in a perforated PTFE tube to avoid galvanic contact with the vessel body. The reference electrode was a custom-built external pressure balanced reference electrode (EPBRE) for HPHT conditions.[25-27] It was based on the Ag/AgCl electrode in saturated KCl solution and was operating at the testing pressure but at room temperature by water cooling. In order to be compatible with the HPHT H_2S environment, the lower part of the EPBRE was packed with fine quartz sand, which served as a diffusion barrier to prevent H_2S contamination of the Ag/AgCl electrode. The reference assembly had a potential of –44 mV_{SCE} at room temperature. It was checked against SCE before and after tests to ensure its proper functionality. All of the potentials of the tests are reported with respect to this customized EPBRE at testing conditions.

After the specimen was installed, the sealed vessel was deaerated to remove oxygen and pressure-tested

[†] Trade name.

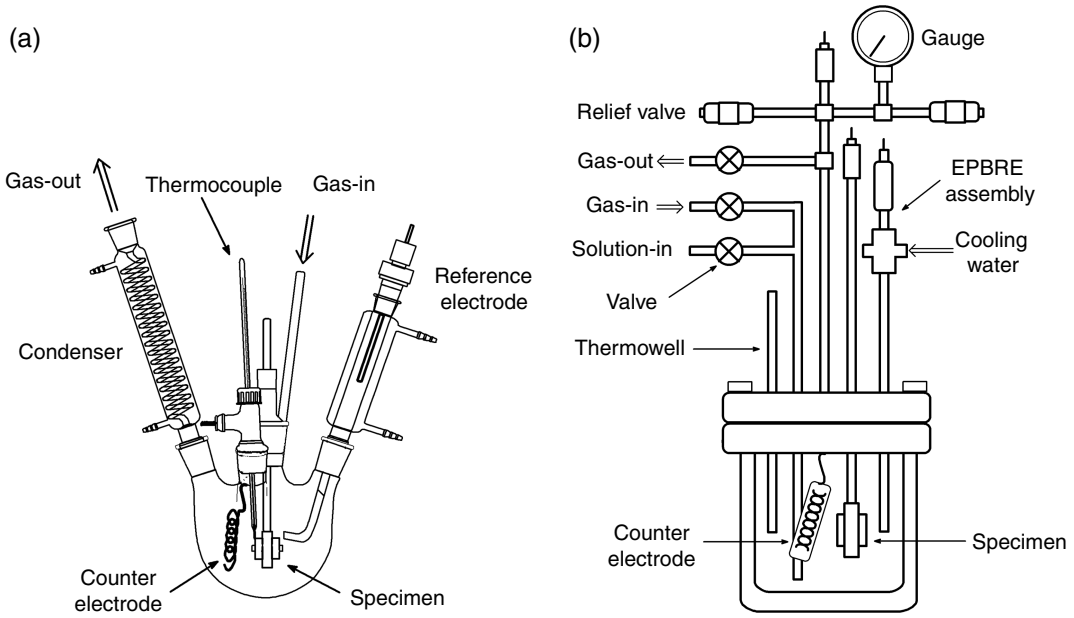

FIGURE 3. *Schematic setup of electrochemical measurement: (a) glass cell at 85°C and (b) pressure vessel at high pressure and high temperature.*

with research grade nitrogen overnight at the testing temperature and pressure. On the second day, the EPBRE assembly was installed on the vessel as long as it did not leak during the pressure test. Then, a preconditioning glass cell was connected to the vessel and about 180 mL of thoroughly deaerated test solution was pressurized into the vessel under nitrogen, leaving approximately one-quarter of vessel volume as overhead vapor space. Nitrogen was kept purging through the entire vessel to completely remove any residual oxygen for about 2 h while the sample OCP was monitored. When the sample OCP gradually decreased and finally stabilized, H_2S mixtures were introduced to the target partial pressure at room temperature. At least 30 min were allowed for the solution to saturate with the gas phase. Sometimes, it was necessary to recharge back to the target partial pressure or to boost with nitrogen to target total pressure. The sample OCP was monitored overnight while the vessel was heated up and maintained at the testing temperature and pressure. Electrochemical tests were performed on the third day when sample OCP reached steady state.

There are a couple of widely used and well-documented electrochemical techniques to identify E_{rp}, i.e., the cyclic potentiodynamic polarization (CPP) and Tsujikawa-Hisamatsu Electrochemical Test (THE, also known as potentiodynamic-galvanostatic-potentiostatic test), as per ASTM Standard G61[28] and ASTM Standard G192,[23] respectively. The E_{rp} value of CRAs decreases with an increase in total charge density, and attains an asymptotical lower-bound value which corresponds to stable pit/crevice growth in the critical occluded environment.[16,29] In order to reach a sufficient total charge density and thus a conservative E_{rp}, the forward scan of CPP has to sweep to a high potential, which frequently results in transpassive dissolution of CRAs and thus affects subsequent E_{rp} determination. Therefore, the CPP method is usually not an ideal method for mild environments. The THE method overcomes these drawbacks and renders conservative and consistent results, especially in less aggressive environments. Its intermediate galvanostatic step allows stable growth of localized corrosion at lower anodic potential. However, the trade-off of the THE method is that it is a time consuming process. In contrast to the CPP method, which can be completed in a few hours, a THE test usually takes over 24 h.

A number of electrochemical methods to measure E_{rp} have been compared in the literature,[30-33] and a number of variant methods have been tried to combine the benefits of the CPP and THE techniques, such as potentiodynamic-potentiostatic-potentiodynamic (PD-PS-PD),[30,32] and potentiodynamic-galvanostatic-potentiodynamic (PD-GS-PD).[31,33] The purpose of the intermediate step, either potentiostatic or galvanostatic holding, is to ensure critical local chemistry formation and the stable growth of localized corrosion, thus rendering a conservative E_{rp}. The series of step-down potentiostatic holding in THE method is replaced by a reverse potentiodynamic scan, which generates comparable results in a relatively short time. In this work, PD-PS-PD technique was primarily used to generate cyclic-like polarization curves and conservative E_{rp} along with a quick CPP method. Nevertheless, the THE method was selectively applied to confirm E_{rp} values. The potentiodynamic scanning was started from –0.1 V_{OCP} to 1 $V_{reference}$, at a scanning rate of

0.167 mV/s. The forward scan reversed at 1 mA/cm^2 in the CPP method, or stopped at a potential in the PD-PS-PD method where an abrupt anodic current increase was observed as indication of localized corrosion initiation. In the following step, the sample was statically held at that potential to ensure at least 2 C/cm^2 total charge density passed through the specimen. The total charge during the intermediate potentiostatic step of PD-PS-PD was controlled by altering the holding duration. The reverse scan was subsequently conducted at 0.167 mV/s until –0.1 V_{OCP} was reached. Solution resistance was obtained from electrochemical impedance spectroscopy before and after electrochemical measurements in low NaCl concentrations for post-measurement IR compensation when IR drop was too large to identify accurate E_{rp} values.

After the electrochemical tests, the cell/vessel was cooled down to room temperature. Both the purging gas and the pressurized H_2S mixtures were filtered through a scrubber filled with 12% NaOH before venting into the fume hood. Nitrogen was subsequently purged through the entire gas-flow path to remove residual H_2S before opening and cleaning the cell/vessel. The removed specimens were then rinsed and ultrasonicated with deionized water for visual inspection with optical microscope to confirm localized corrosion.

Electrochemical tests on the S13Cr SS and Alloy 2535 specimens were extensively repeated (more than twice) to provide reliable E_{rp} data for developing the model parameters. The tests on DSS 2507 and Alloy 29 were repeated as needed for further confirmation. Because of their close chemical composition to other alloys, S15Cr SS and Alloy 28 were spot-checked as a blind test against E_{rp} model prediction optimized for S13Cr SS, Alloy 2535, and Alloy 29.

COMPUTATIONAL MODEL

In a previous study,[22] a mechanistic model had been derived for calculating the repassivation potential of alloys in aqueous environments containing chlorides and hydrogen sulfide. The model relates the repassivation potential to the activities of solution species and temperature based on the following assumptions:

(i) The metal (M) undergoes dissolution underneath a layer of concentrated metal halide solution MX. The concentrated solution may or may not be saturated with respect to a hydrous solid metal halide salt film.
(ii) In the process of repassivation, a thin layer of metal oxide (MO) is assumed to form at the interface between the metal and the hydrous metal halide.
(iii) At a given instant, the oxide layer covers a certain fraction of the metal surface. This fraction increases as repassivation is approached.
(iv) The dissolution rate of the metal under the oxide is lower than at the metal/halide interface and corresponds to the passive dissolution rate. Thus, as the repassivation potential is approached, the dissolution rate tends toward the passive dissolution rate.
(v) The model is one-dimensional, i.e., the fluxes of solution species and metal ions are considered in one dimension.
(vi) The model includes the effects of multiple species, which adsorb competitively on the metal surface.
(vii) The aggressive species form adsorbed metal complexes, which dissolve in the active state.
(viii) H_2S may have dual effect, i.e., it can accelerate the anodic dissolution in the active state via the formation of adsorbed species or it can inhibit the dissolution through the formation of sparingly soluble metal sulfide (MS) species. The solid MS species form in competition with the MO species.
(ix) Repassivation is reached when the current density reaches a predetermined low value i_{rp} (assumed to be $i_{rp} = 10^{-2}$ A/m^2). At the same time, the fluxes of metal ions become small and comparable to those for passive dissolution.

Although the equations that describe these processes are complex and can be, in general, solved only numerically, a closed-form equation has been found in the limit of repassivation. As the derivation of the model was described previously,[22] the final equations are summarized here and introduce the parameters that need to be evaluated to apply the model in practice. For a system that contains chloride ions with the activity of a_c and dissolved hydrogen sulfide with the activity of a_s in the bulk solution, E_{rp} is calculated by solving the following equation:

$$i_{rp} = \frac{(i_c^0 r_c a_c + i_{MO}^0)(1 + e_{MS} i_{MS}^0) + (i_{MS}^0 + i_s^0) r_s a_s}{\left[1 + r_c a_c + \frac{i_{MO}^0}{i_p}\right](1 + e_{MS} i_{MS}^0) + r_s a_s \left(1 + \frac{i_{MS}^0}{i_q (1 + u_{MS} a_s)}\right)} \quad (1)$$

with the quantities i_c^0, i_s^0, i_{MO}^0, and i_{MS}^0 defined as:

$$i_c^0 = f_c \exp\left[\frac{\alpha_c F E_{rp}}{RT}\right] \quad (2)$$

$$i_s^0 = f_s \exp\left[\frac{\alpha_s F E_{rp}}{RT}\right] \quad (3)$$

$$i_{MO}^0 = f_{MO} \exp\left[\frac{\xi_{MO} F E_{rp}}{RT}\right] \quad (4)$$

$$i_{MS}^0 = f_{MS} \exp\left[\frac{\xi_{MS} F E_{rp}}{RT}\right] \quad (5)$$

where the subscripts c, s, MO, and MS denote the adsorbed Cl^-, adsorbed H_2S, solid metal oxide, and solid metal sulfide, respectively; f_c and f_s are the pre-exponential rate constants for the current densities for the anodic dissolution mediated by the adsorption of Cl^- and H_2S, respectively; α_c and α_s are the corresponding electrochemical transfer coefficients for these processes; f_{MO} and f_{MS} are the pre-exponential rate constants for the current densities for the formation of MO and MS, respectively; ξ_{MO} and ξ_{MS} are the corresponding electrochemical transfer coefficients; r_c and r_s are the adsorption equilibrium constants for Cl^- and H_2S, respectively; e_{MS} is the coupling constant that relates the rate of surface coverage growth of MS to the corresponding current density; i_p is the passive current density; i_q is the current density for the dissolution of a surface covered with the sulfide MS; and u_{MS} is the dissolution rate of solid MS.

In a practical implementation, the rate constants f_j (j = c, MO, MS, or s) in Equations (2) through (5) are expressed using corresponding Gibbs energies of activation, i.e.:

$$f_j = \exp\left(-\frac{\Delta g_j^{\neq}}{RT}\right) \quad (6)$$

An analogous equation expresses the dissolution rate constant u_{MS} in terms of a corresponding Gibbs energy of activation, $\Delta g^{\neq}_{dis,MS}$, i.e.:

$$u_{MS} = \exp\left(-\frac{\Delta g^{\neq}_{dis,MS}}{RT}\right) \quad (7)$$

The Gibbs energy of activation may be temperature-dependent according to the relation:

$$\frac{\Delta g_j^{\neq}}{RT} = \frac{\Delta g_j^{\neq}(T_{ref})}{RT} + \Delta h_j^{\neq}\left(\frac{1}{T} - \frac{1}{T_{ref}}\right) \quad (8)$$

where T_{ref} is the reference temperature (T_{ref} = 298.15 K), and $\Delta g_j^{\neq}(T_{ref})$ and $\Delta h_j^{\neq}$ are the Gibbs energy of activation at T_{ref} and enthalpy of activation, respectively. The adsorption equilibrium constants are expressed using a Gibbs energy of adsorption, i.e.:

$$r_j = \exp\left(-\frac{\Delta g_{ads,j}}{RT}\right) \quad (9)$$

where j = c and s, and the Gibbs energy of adsorption, $\Delta g_{ads,j}$, is assumed to be independent of temperature. The coefficient f_s in Equation (3) is related to the activity of chlorides as:

$$f_s = f_s' a_c \quad (10)$$

The coefficients f_j (j = c, MO, and MS) and f_s' depend on temperature according to Equations (6) and (8). The remaining model parameters have universal values. Specifically, the electrochemical transfer coefficients in Equations (2) and (3) are equal to 1, i.e.:

$$\alpha_c = \alpha_s = 1 \quad (11)$$

and the electrochemical transfer coefficients for the formation of the solids, MO and MS, (Equations [4] and [5]) have a common value as determined previously:[34]

$$\xi_{MO} = \xi_{MS} = 0.8 \quad (12)$$

Further, the constants i_p and i_q in Equation (1) are assigned the value of 10^{-4} A/m^2, which is a reasonable approximation of the passive current density[20] of CRAs. The coupling parameter e_{MS} is equal to 0.001 as determined earlier.[22]

Following previous work,[20,34] the activities of Cl^-, a_c, and those of H_2S, a_s, are calculated from an electrolyte thermodynamic model.[35-36] At the conditions investigated here, H_2S exists in the aqueous phase predominantly in the form of a neutral species $H_2S_{(aq)}$ and, therefore, there is no need to include other sulfur-bearing species in the E_{rp} model.

For a consistent application of the model, it is necessary to use a uniform potential scale over the complete range of temperatures investigated here. Therefore, all potentials are calculated with respect to the standard hydrogen electrode (SHE) at the experimental temperature. The conversion between the SHE scale in the model and the reference electrodes scales (both SCE and customized EPBRE) as used in the experimental measurements has been described elsewhere.[22,37]

RESULTS AND DISCUSSION

Determination of E_{rp}

Electrochemical measurements were initially performed on cylindrical coupons. As a result of fluctuation of liquid/gas interface caused by gas sparging, noisy results were frequently observed on cylindrical coupons. In addition, significant corrosion at liquid/gas interface was also noticed, which led to inconsistent E_{rp} measurement. Fully submerged crevice specimens exhibited less noisy curves and more conservative E_{rp} values than the partially submerged cylindrical coupons. Therefore, crevice specimens were preferred for electrochemical tests to determine E_{rp} values for CRAs.

In sour environments, the presence of H_2S can interfere with the electrochemical measurement. Oxidation of H_2S causes an increase of the total anodic current at a characteristic potential, which depends on H_2S solubility in the solution, temperature, and material surface properties. Especially in the environment of high H_2S and low chloride, metal dissolution is typically masked by the background of H_2S oxidation

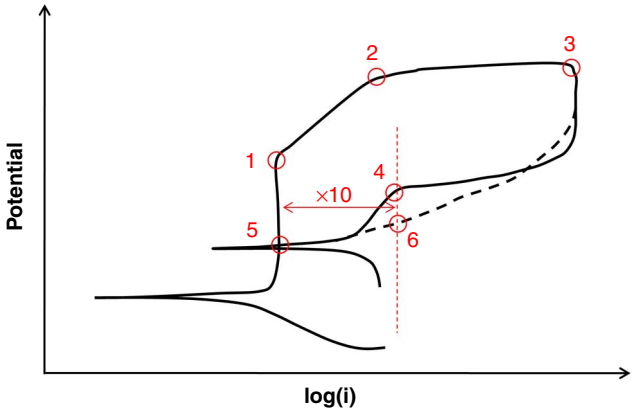

FIGURE 4. *Illustration of critical points in the polarization curve and the approach to determine E_{rp} in the presence of an inflection point on the reversed scan.*

current, which makes it difficult to detect the onset of localized corrosion and repassivation. Nevertheless, a scenario of high H_2S and low chloride is most unlikely to occur in oil and gas production environments.

A systematic approach to determine E_{rp} values of CRAs has been developed in this work. Figure 4 shows a typical schematic potentiodynamic polarization loop of a CRA in the $Cl^- + H_2S$ system, generated by CPP or PD-PS-PD methods. A forward scan starts from −100 mV_{OCP} and the applied potential sweeps toward positive direction. After passing the zero current point, also known as corrosion potential (E_{corr}), the anodic current density remains at a ~$\mu A/cm^2$ level regardless of the potential increase. This represents the classic passivation behavior and excellent corrosion resistance. When the potential reaches the point #1, the anodic current density log(i) tends to increase with a near-Tafel behavior with regard to potential E. This overpotential driven process results from H_2S oxidation, which normally occurs from –300 mV_{SCE} to –200 mV_{SCE} in the test environment at 85°C. The potential of the deflection point #1 (indicated as $E_{H_2S}^{redox}$, which is not identical to the reversible potential of H_2S oxidation, but close) is a function of dissolved H_2S concentration and temperature, and occurs at lower potentials for higher H_2S concentration. Moreover, the occurrence of point #1 also depends on the sample E_{corr}. In a low-chloride solution, E_{corr} can be higher than the potential of H_2S oxidation. In this case, the passive region disappears and the anodic polarization branch displays an active Tafel behavior dominated by H_2S oxidation. If the availability of H_2S species at the sample surface is limited by a mass transport process, log(i) may deviate from linear Tafel behavior with respect to potential E and the slope increases. Localized corrosion of CRAs can be normally initiated in the potential region higher than the H_2S oxidation potential.

The onset of localized corrosion is normally characterized by an abrupt anodic current increase. In regions 2 and 3, localized metal dissolution typically causes a rapid increase in the current and the slope decreases. A distinctive point #2 may not be evident when the local metal dissolution current is much smaller than the H_2S oxidation current. Either the potentiostatic step in PD-PS-PD method or the galvanostatic step in THE method should be retained in this region. A gradually increasing anodic current at a potentiostatic holding step is considered as confirmation of stable pit/crevice growth. A reverse scan normally starts from point #3, at the same potential or the last potential in the galvanostatic step. Localized corrosion is further confirmed by visual observation of sample surface after tests with optical microscope.

In traditional electrochemical experiments and standards,[28] the intersection point of the reverse scan with the forward scan is normally regarded as E_{rp} (point #5 in Figure 4). However, it has been found that this approach results in an over-conservative evaluation of E_{rp}. In the present work on CRAs, an inflection point was frequently observed in the reverse scans, as illustrated by point #4. This indicates the change of electrochemical kinetics, i.e., the onset of repassivation. The inflection point #4 is typically within 10 times of the passive current density. Point #4 is not considered as the cessation of localized corrosion if it is in the high current density region, which could be a result of the reduction of other oxidized species in solution. In some cases, when the inflection point #4 was not distinctly revealed in the reverse scan (such as the dashed line illustrated in Figure 4), E_{rp} was then systematically defined at the intersection point #6 of the reverse scan with the vertical line of 10 times the passive current density (dotted line in red). If there was no distinguishable passive region, which was normally the case at low chloride conditions, E_{rp} was arbitrarily chosen at the current density of 10^{-5} A/cm^2 for the temperature of 85°C, and 10^{-4} A/cm^2 for temperatures higher than 100°C. The procedure for E_{rp} determination is summarized in the flow chart in Figure 5.

The E_{rp} value can be further confirmed by other electrochemical approaches, i.e., by potentiostatic experiments without showing any localized attack for 24 h at a potential 50 mV lower than the inflection point value, and the THE method showing a current transition from increasing to decreasing at potentiostatic holding steps. THE technique is more deterministic in confirming E_{rp} than potentiostatic holding because it is still debatable whether a 24-h duration time in a potentiostatic test is long enough to draw a conclusion regarding the resistance to localized corrosion. On the other hand, the THE method is also limited in discerning metal dissolution from the background of H_2S oxidation current.

Electrochemical Results

The effect of H_2S on the electrochemical properties of CRAs is complex, as a result of the influence of its

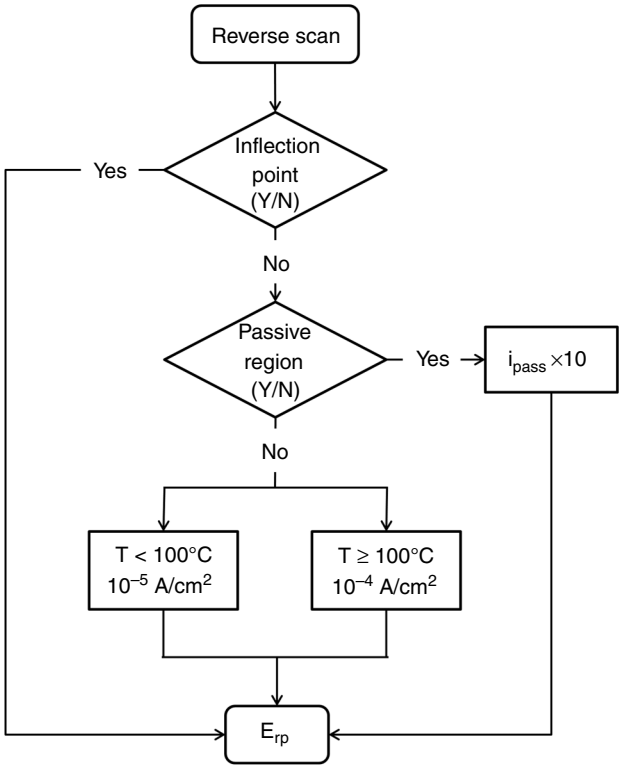

FIGURE 5. *A flow chart illustrating the process of E_{rp} determination for CRAs in this work.*

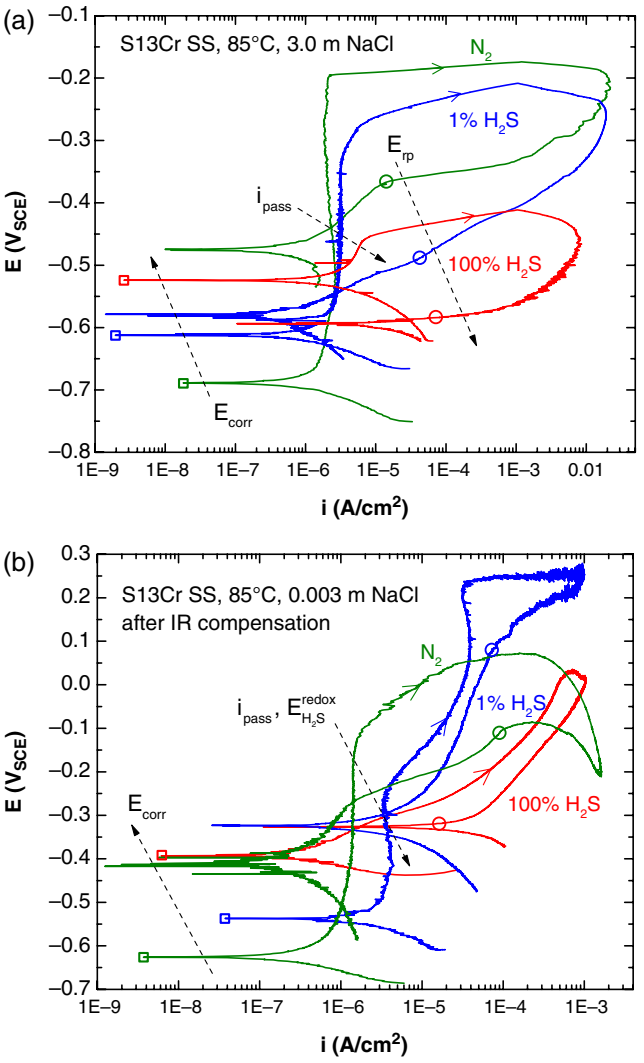

FIGURE 6. *Electrochemical polarization curves of S13Cr SS in deaerated (a) 3.0 m NaCl and (b) 0.003 m NaCl at 85°C as a function of H_2S concentration in the gas phase. Corrosion potentials and the determined repassivation potentials are marked as open squares and open circles, respectively.*

oxidation process and its double role in the active dissolution and passivation process. The polarization curves of S13Cr SS at 85°C in a 3.0 m NaCl solution are shown in Figure 6(a). Here, the high chloride solution is such an aggressive environment that localized corrosion can be initiated regardless of the presence of H_2S oxidation. At this condition, the corrosion potential (E_{corr}) increases as a result of the fact that the dissolved H_2S also behaves as a weak acid in aqueous solutions. The passive current density (i_{pass}) is largely of the order of μA/cm^2, and slightly increases with dissolved H_2S. The E_{rp} values determined from polarization curves consistently decrease with H_2S concentration.

At lower chloride concentrations, i.e., below 0.3 m, the oxidation of H_2S interferes with experiments performed on S13Cr SS, where the onset of localized corrosion and repassivation occur under the influence of H_2S oxidation. For instance, the polarization curves of S13Cr SS in 0.003 m NaCl solution at 85°C are shown in Figure 6(b). In contrast to the increase of E_{corr} with dissolved H_2S concentration, the redox potential of H_2S on the sample surface decreased. Post-measurement compensation of ohmic potential has to be applied because the solution resistance at such concentration is not negligible and thus generates a significant IR drop. When metal dissolution is considerable and therefore leads to an increase of ionic concentration in the solution, over-compensation sometimes occurs, as shown as the bend-down of the curve in the high current density region. In the case of 1% H_2S, the transition from the anodic current dominated by H_2S oxidation to that dominated by localized corrosion was clearly shown in the 250 mV_{SCE} region. The inflection point in the reverse scan is at about 80 mV_{SCE}, considered as E_{rp}, which is even higher than that in the H_2S-free condition. All of this suggests a better resistance to localized corrosion of S13Cr SS with a small amount of H_2S in a dilute chloride environment, as a result of competing processes of stable protective sulfide film formation and dissolution of protective oxide layer. In the case of 100% H_2S, the corrosion potential of S13Cr SS is close to the H_2S oxidation potential. The anodic forward scan quickly entered the region where H_2S oxidation

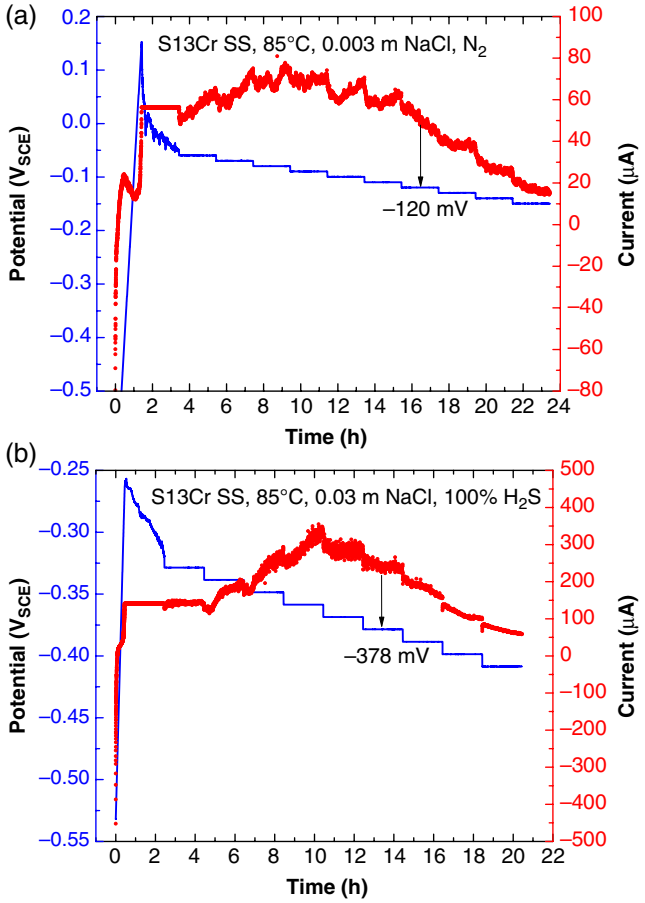

FIGURE 7. *The results to confirm the repassivation potential value of S13Cr SS in (a) deaerated 0.003 m NaCl and (b) deaerated 0.03 m NaCl saturated with 100% H_2S at 85°C. The potential that corresponds to the first descending current in the potentiostatic step is considered as E_{rp} and matches the E_{rp} values obtained from polarization curves in the same conditions.*

was the dominant process in the absence of a typical passive region.

The E_{rp} values obtained from polarization curves in low chloride conditions were further confirmed with THE tests. Examples of THE results obtained in low chloride environments are shown in Figure 7 and provide comparable E_{rp} values to those obtained with the PD-PS-PD method. The first potential at which the anodic current started to decrease consistently showed comparable values to the E_{rp} values determined from polarization curves by the procedure introduced previously. However, it is still debatable whether THE is an effective technique to reveal a conservative E_{rp} of CRAs in the high-H_2S but dilute chloride environments, where the H_2S oxidation current dominates the measured anodic current. At potentiostatic stepping-down, the decrease of total anodic current does not always reflect the decrease of metal dissolution, which could be caused by the surface barrier of H_2S oxidation products and a mass transport limiting process. As a result of overwhelming H_2S oxidation, the E_{rp} defined in this condition is easily close to the potential where H_2S oxidation starts or ceases. It is challenging to determine a convincing E_{rp} solely by electrochemical measurements on the bulk sample. Some research work on a 1D artificial pit (lead-in-pencil electrode) has been tried to solve this problem.[38] After all, the extremely low chloride and high H_2S scenario seldom occurs in oil and gas production. The electrochemical polarization loop and THE method are still effective experimental techniques to reveal the critical potential $-E_{rp}$ in most cases.

Super-DSS 2507 has a higher content of Ni, Cr, Mo, and N than S13Cr SS, which translates into better corrosion resistance as indicated by its higher PRE_N. In comparison to S13Cr SS in 3.0 m NaCl solution, the i_{pass} is almost 10 times smaller, and the initiation potentials of localized corrosion are around 300 mV higher, as shown in Figure 8(a). The presence of H_2S enhances localized corrosion and decreases E_{rp} as expected. In contrast, a high concentration of H_2S has a more significant effect on the increase in i_{pass}, but the i_{pass} is still a few times smaller than in the case of S13Cr SS in the same environment. Further, 1% H_2S does not exhibit a significant inhibitive effect in dilute chloride solutions. In the dilute NaCl solution, as shown in Figure 8(b), E_{corr} is raised to the vicinity of the H_2S oxidation potential, and thus the passive region is not distinguishable. The bi-phase structure of DSS 2507 adds a complexity resulting from the slight differences in alloying element compositions and microstructure between the ferrite and austenite phases. In general, localized corrosion first initiates in the ferrite phase, and thus the actual resistance to localized corrosion is closely related to the galvanic interaction between the two constituent phases rather than to the individual pitting/crevice resistance of the two phases.[39]

The Ni-based Alloy 2535 has a higher Ni content, which introduces additional complexities in its electrochemical properties in H_2S-containing environments. It has been found that nickel has a strong adsorption and catalytic effect with H_2S and elemental sulfur,[40-41] which diminishes the effect of H_2S concentration and influences the repassivation process. As shown in Figure 9, the dissolved H_2S increases E_{corr} and decreases E_{rp} in NaCl solutions at 85°C. However, it is interesting to find that i_{pass} tends to decrease slightly with H_2S concentration. At 232°C, as shown in Figure 10, i_{pass} is over an order of magnitude higher than that at 85°C, and the effect of H_2S concentration on E_{rp} becomes smaller. It can be noticed that the area of the polarization loop becomes smaller and even a positive hysteresis exists at 232°C. The decrease in anodic current is caused by the formation of a barrier of H_2S oxidation products and corrosion products, which was confirmed by post-measurement visual inspection.

As shown in Figures 11 and 12, Alloy 29 exhibits a similar electrochemical behavior to Alloy 2535 at low

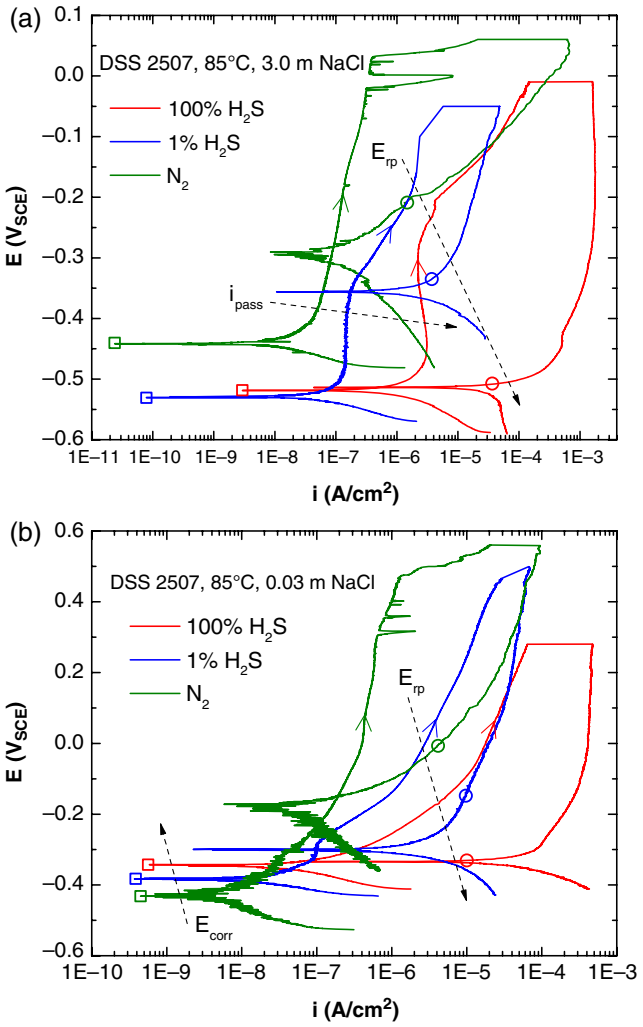

FIGURE 8. *Electrochemical polarization curves of DSS 2507 in deaerated (a) 3.0 m NaCl and (b) 0.03 NaCl at 85°C as a function of H_2S concentration in the gas phase. Corrosion potentials and the determined repassivation potentials are marked as open squares and open circles, respectively.*

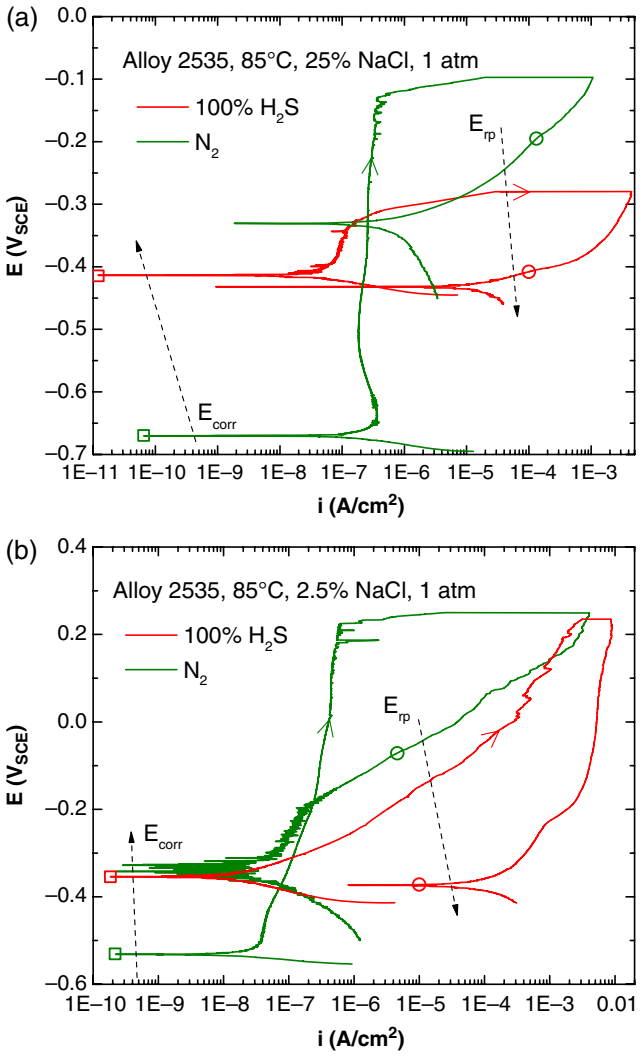

FIGURE 9. *Electrochemical polarization curves of Alloy 2535 in deaerated (a) 25% NaCl and (b) 2.5% NaCl at 85°C as a function of H_2S concentration in the gas phase. Corrosion potentials and the determined repassivation potentials are marked as open squares and open circles, respectively.*

and high temperatures. A slightly better localized corrosion resistance than for Alloy 2535 results from its higher Cr and Mo content.

Finally, all of the E_{rp} values generated in the experimental work are summarized in Table 3. A set of E_{rp} data for S13Cr SS has been reported in the previous work.[22]

Determination of Model Parameters

In the first step, the parameters of the model have been determined for the alloys in chloride-only environments because such environments provide a baseline for analyzing the effect of H_2S. In Cl^- systems, the model is fully defined by five adjustable parameters: the Gibbs energy $\Delta g_c^{\neq}(T_{ref})$ and enthalpy $\Delta h_c^{\neq}$ of activation for the anodic dissolution mediated the adsorption of Cl^- ions (Equations [2], [6], and [8]), the Gibbs energy $\Delta g_{MO}^{\neq}(T_{ref})$ and enthalpy $\Delta h_{MO}^{\neq}$ of activation for the formation of the oxide (Equations [4], [6], and [8]), and the Gibbs energy of adsorption of Cl^- ions $\Delta g_{ads,c}$ (Equation [9]). For the alloys studied here, $\Delta g_{MO}^{\neq}(T_{ref})$, $\Delta h_{MO}^{\neq}$, ξ_{MO}, and $\Delta g_{ads,c}$ have been obtained by utilizing the previously developed generalized correlation[34] and only the two remaining parameters (i.e., $\Delta g_c^{\neq}(T_{ref})$ and $\Delta h_c^{\neq}$) have been adjusted to match the data. All model parameters are listed in Table 4. With these parameters, the model accurately reproduces the experimental E_{rp} data in H_2S-free systems as a function of Cl^- concentration and temperature. This is illustrated in Figures 13 through 15 (cf. the hollow circles and green lines for Cl^--only systems). It should be noted that the generalized correlation[34] can also predict the parameters $\Delta g_c^{\neq}(T_{ref})$ and $\Delta h_c^{\neq}$. However, it is

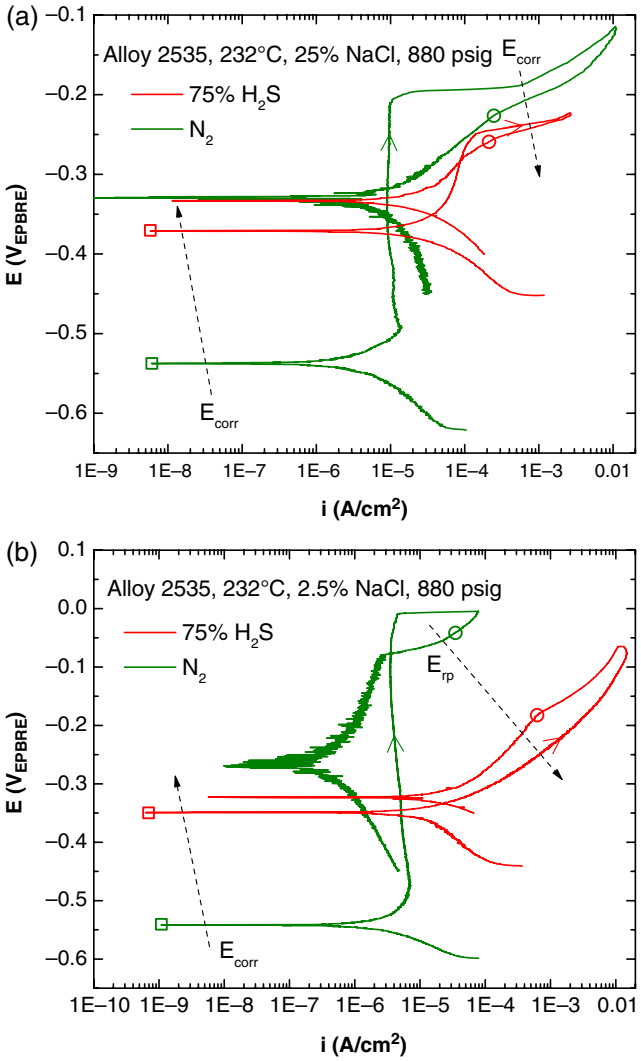

FIGURE 10. *Electrochemical polarization curves of Alloy 2535 in deaerated (2) 25% NaCl and (b) 2.5% NaCl at 232°C as a function of H_2S concentration in the gas phase. Corrosion potentials and the determined repassivation potentials are marked as open squares and open circles, respectively.*

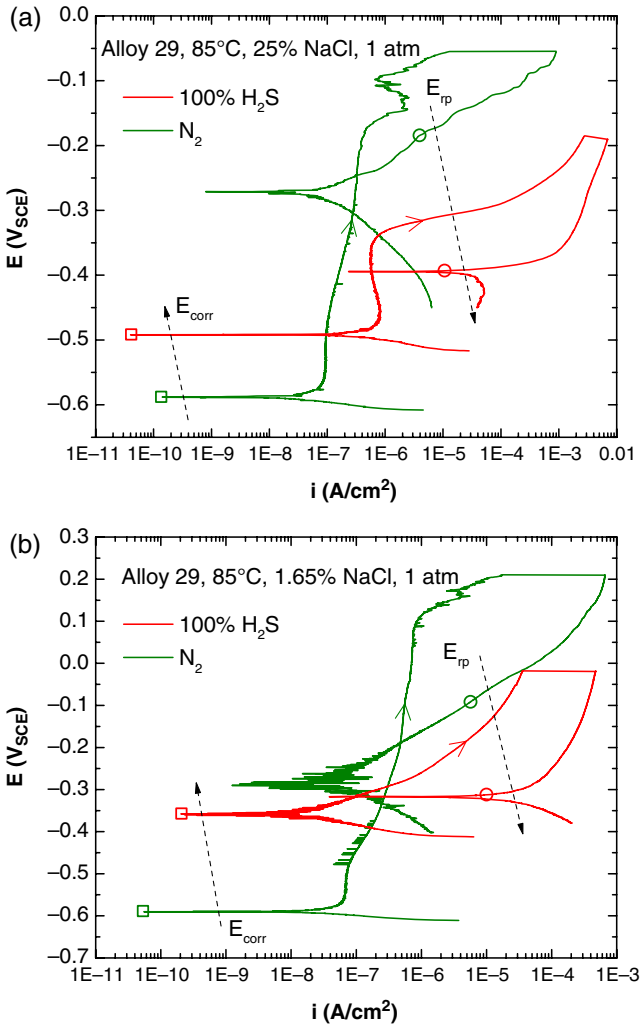

FIGURE 11. *Electrochemical polarization curves of Alloy 29 in deaerated (a) 25% NaCl and (b) 1.65% NaCl (10,000 ppm Cl^-) at 85°C as a function of H_2S concentration in the gas phase. Corrosion potentials and the determined repassivation potentials are marked as open squares and open circles, respectively.*

preferred to adjust these parameters if experimental data in Cl solutions are available.

In the second step, model parameters have been determined for H_2S-containing systems. These parameters include the Gibbs energy of adsorption of H_2S ($\Delta g_{ads,s}$) and the Gibbs energies of activation for H_2S-accelerated dissolution, metal sulfide formation, and sulfide chemical dissolution ($\Delta g^{\neq}_{s}(T_{ref})$, $\Delta g^{\neq}_{MS}(T_{ref})$, and $\Delta g^{\neq}_{dis,MS}$, respectively). Remarkably, the enthalpies of activation for H_2S-accelerated dissolution and metal sulfide formation (cf. Equation [8]) have been determined to be zero for the alloys for which data are available at higher temperatures. This is a practically important result as it facilitates the use of the model as a tool for extrapolating the data to higher temperatures.

The four H_2S-related parameters show highly regular behavior, thus facilitating their determination. Specifically, $\Delta g_{ads,s}$ can be assigned a common value for all of the alloys investigated here, i.e., $\Delta g_{ads,s}$ = −11 kJ/mol. Because this parameter reflects the energetics of H_2S adsorption, its value determines the sensitivity of the H_2S-induced depression of E_{rp} to the concentration of dissolved H_2S. Further, the $\Delta g^{\neq}_{dis,MS}$ parameter can be expected to have a common value because it reflects the energetics of the dissolution of metal sulfides, which are dominated by nickel sulfide in CRAs.[42] Thus, the value obtained in a previous study for S13Cr SS[22] has been adopted for all alloys. This leaves two alloy-specific parameters, i.e., $\Delta g^{\neq}_{s}(T_{ref})$ and $\Delta g^{\neq}_{MS}(T_{ref})$. Because $\Delta g^{\neq}_{s}(T_{ref})$ quantifies the kinetics of H_2S-mediated acceleration of anodic dissolution and $\Delta g^{\neq}_{MS}(T_{ref})$ quantifies the kinetics of formation of a protective MS sulfide layer, it is reasonable to assume

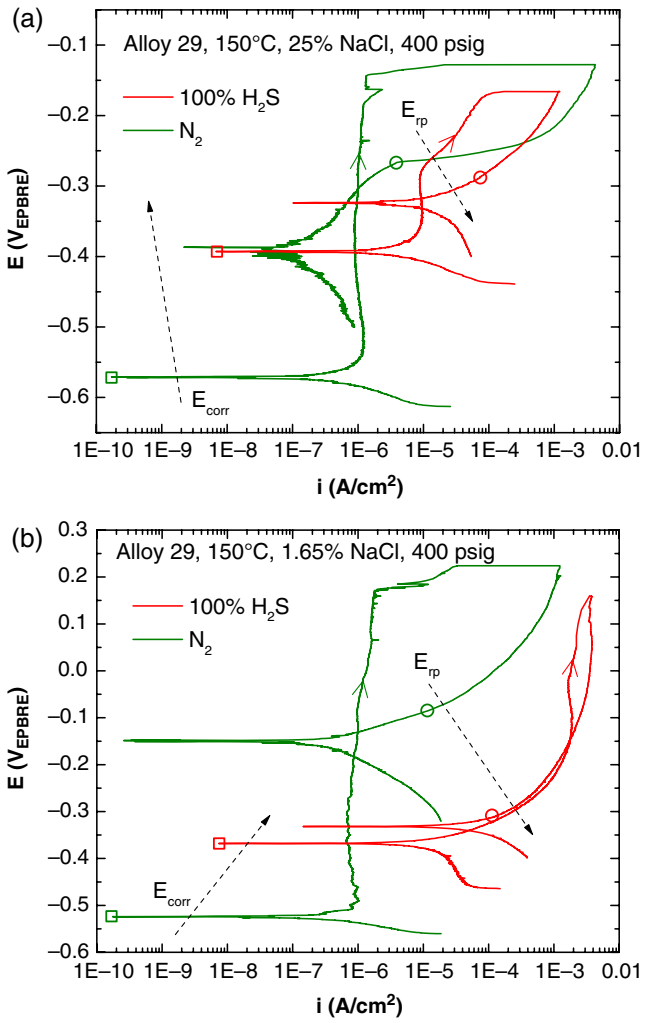

FIGURE 12. *Electrochemical polarization curves of Alloy 29 in deaerated (a) 25% NaCl and (b) 1.65% NaCl (10,000 ppm Cl^-) at 150°C as a function of H_2S concentration in the gas phase. Corrosion potentials and the determined repassivation potentials are marked as open squares and open circles, respectively.*

that these two parameters are correlated for similar alloys because they reflect two pathways of metal-adsorbed sulfur reactions. Indeed, analysis of these parameters obtained for individual alloys reveals that a linear correlation between $\Delta g_s^{\neq}(T_{ref})$ and $\Delta g_{MS}^{\neq}(T_{ref})$ exists, i.e., $\Delta g_{MS}^{\neq}(T_{ref}) = 1.2\Delta g_s^{\neq}(T_{ref}) + 25.38$. Thus, the influence of H_2S on E_{rp} can be effectively modeled using only one independent parameter, i.e., $\Delta g_s^{\neq}(T_{ref})$. Furthermore, this parameter can be linearly correlated with $\Delta g_c^{\neq}(T_{ref})$ in order to estimate it for alloys for which no experimental data are available. The optimum values of the model parameters for the six investigated alloys are listed in Table 4. It should be noted that selected parameters for S13Cr SS have been modified compared to those reported earlier[22] because a comparably accurate representation of the data can be obtained using a common value of the Gibbs energy of adsorption (i.e., $\Delta g_{ads,s} = -11$ kJ/mol).

Repassivation Potential Modeling Results

In general, the model can be used in two modes, i.e., (1) as a tool to reproduce and extrapolate the available experimental data as a function of environmental conditions or (2) as a tool to estimate E_{rp} for alloys that have not been experimentally investigated or have been studied to a limited extent. In the latter case, the previously developed E_{rp} correlation[34] is utilized to estimate the parameters for chloride systems (i.e., $\Delta g_c^{\neq}(T_{ref})$, $\Delta h_c^{\neq}$, $\Delta g_{MO}^{\neq}(T_{ref})$, and $\Delta h_{MO}^{\neq}$) and the H_2S-related parameters are estimated as described earlier. In the case of alloys S13Cr, 2507, 2535, and 29, a sufficient amount of experimental data has been generated to determine the model parameters and establish the regularities for the H_2S-related parameters. For S15Cr SS and Alloy 28, more limited data are available. Therefore, these two alloys were used to test the model in the estimation mode.

Figure 13 compares the calculated and experimental repassivation potentials for alloys S13Cr, 2507, 2535, and 29 at 85°C. For each alloy, the results are shown for three H_2S concentrations in the gas phase, i.e., for 0% H_2S (green lines and circles), an intermediate concentration of 1% H_2S for S13Cr SS and DSS 2507 (blue lines and triangles), and 100% H_2S (red lines and diamonds). Also, calculated results are included for Alloys 2535 and 29 in the presence of 10% H_2S. The model accurately represents the experimental data and quantitatively captures the complexity of the H_2S effect.

Figure 14 compares the predictions with the data for the two alloys that were used as test cases, i.e., S15Cr SS and Alloy 28. In the case of S15Cr SS, both the Cl^--related and H_2S-related parameters have been estimated, thus resulting in a complete prediction. However, in the case of Alloy 28, an adjustment of the $\Delta g_c^{\neq}(T_{ref})$ and $\Delta h_c^{\neq}$ parameters has been made based on the data in Cl^--only solutions. This was a result of the fact that the generalized correlation for chloride systems[34] predicts that the E_{rp} of Alloy 28 is slightly higher than that of Alloy 2535 because of a higher Cr and Mo content in Alloy 28. However, the available data indicate the opposite, i.e., the experimental E_{rp} of Alloy 28 is lower than that of Alloy 2535 (cf. a further discussion of the effect of alloying elements later). After the adjustment of the $\Delta g_c^{\neq}(T_{ref})$ and $\Delta h_c^{\neq}$ parameters, the H_2S-related parameters were estimated. As shown in Figure 14, the predictions are consistent with the data for both alloys.

Effects of H_2S

It is evident that the effect of H_2S on the repassivation potential is complex. At high H_2S concentrations (100%), uniform behavior is observed for all alloys (cf. the diamonds and red lines). In this case, the E_{rp} vs. Cl^- curves are almost parallel to those in the absence of H_2S but are shifted toward lower potentials

TABLE 3

Summary of Experimental E_{rp} Values Generated for Selected CRAs

Alloy	Temperature	Reference Electrode	Total Pressure (atm)	Chloride (NaCl)	H_2S (wt%)[A]	E_{rp} (mV_{Ref})	E_{rp} (mV_{SHE})
S15Cr	85°C	SCE	1	0.003 m	0	–173	–20
				0.003 m		–121	32
				0.03 m		–209	–58
				0.3 m		–248	–99
				0.3 m		–244	–95
				0.003 m	1	–20	173
				0.03 m		–168	–17
				0.3 m		–275	–126
				0.03 m	100	–385	–234
				3 m		–570	–424
2507	85°C	SCE	1	0.003 m	0	87	240
				0.03 m		–9	142
				0.3 m		–206	–57
				3.0 m		–210	–64
				0.003 m	1	–89	64
				0.003 m		–33	120
				0.003 m		38	191
				0.03 m		–91	60
				0.03 m		–145	6
				0.3 m		–247	–98
				1.0 m		–320	–172
				3.0 m		–240	–94
				3.0 m		–346	–200
				0.003 m	100	–306	–153
				0.03 m		–331	–180
				0.3 m		–382	–233
				3.0 m		–509	–363
2535	85°C	SCE	1	2.5%	0	–89	60
				25%		–189	–46
				25%		–169	–26
				2.5%	100%	–358	–209
				25%		–403	–260
	232°C	EPBRE	63.6	2.5%	0	–64	–185
			63.6	2.5%		–37	–158
			60.9	2.5%		–38	–159
			62.2	25%		–223	–351
			62.2	25%		–228	–356
			62.2	2.5%	75%	–165	–286
			49.3	2.5%		–126	–247
			66.3	2.5%		–181	–302
			52.0	25%		–267	–388
			60.9	25%		–256	–384
			60.9	25%		–223	–351
29	85°C	SCE	1	1.65%	0	–90	59
				1.65%		–96	53
				25%		–185	–42
				25%		–148	–5
				1.65%	100%	–312	–163
				1.65%		–241	–92
				25%		–393	–250
				25%		–410	–267
	150°C	EPBRE	28.9	1.65%	0	–88	–74
			28.9	1.65%		–73	–59
			28.2	25%		–266	–256
			28.2	1.65%	100%	–191	–178
			37.1	1.65%		–311	–297
			25.5	25%		–280	–273
	200°C	EPBRE	50.0	1.65%	0	–112	–176
			47.3	25%		–181	–253

(*continued*)

TABLE 3 (*Continued*)

Alloy	Temperature	Reference Electrode	Total Pressure (atm)	Chloride (NaCl)	H_2S (wt%)[A]	E_{rp} (mV_{Ref})	E_{rp} (mV_{SHE})
			45.2	1.65%	71%	–230	–294
			47.3	25%		–225	–297
			47.3	25%		–304	–376
28	85°C	SCE	1	25%	0	–279	–136
				25%	100%	–422	–279
	150°C	EPBRE	28.2	25%	0	–281	–274
			27.2	25%	100%	–264	–257
	200°C	EPBRE	45.9	25%	0	–265	–337
			45.2	25%	71%	–209	–281

[A] This was the gas phase composition at room temperature. Before heating up, 250 psig (1.7 MPa) pressurized vessel was used for tests at 150°C; 350 psig (2.4 MPa) pressurized vessel was used for tests at 200°C and 232°C.

TABLE 4
Parameters of the Repassivation Potential Model[A]

Model Parameter	Parameter Definition	Alloy					
		S13Cr	S15Cr	2507	2535	29	28
$\Delta g_c^{\neq}(T_{ref})$	Gibbs energy of activation for dissolution mediated by adsorption of Cl^- at reference T	–9.16	–5.34	9.02	13.5	17.6	1.7
$10^{-3}\ \Delta h_c^{\neq}$	Enthalpy of activation for dissolution mediated by adsorption of Cl^-	0.018	0.025	0.057	0.058	0.076	0.036
$\Delta g_{ads,c}$	Gibbs energy of adsorption of Cl^-	10					
$\Delta g_{MO}^{\neq}(T_{ref})$	Gibbs energy of activation for oxide formation at reference temperature	25	25	15.8	20.5	21	15.5
$10^{-3}\ \Delta h_{MO}^{\neq}$	Enthalpy of activation for oxide formation	–0.010	–0.010	–0.085	–0.070	–0.070	–0.070
$\Delta g_s^{\neq}(T_{ref})$	Gibbs energy of activation for dissolution mediated by adsorption of H_2S at reference T	–23.7	–20.5	–13.4	–8.6	–7.6	–9.1
$\Delta g_{ads,s}$	Gibbs energy of adsorption of H_2S	–11					
$\Delta g_{MS}^{\neq}(T_{ref})$	Gibbs energy of activation for sulfide formation at reference T	–2.7	0.67	9.3	15.1[B]	16.3[B]	14.5[B]
$\Delta g_{dis,MS}^{\neq}$	Gibbs energy of activation for sulfide dissolution	–21.4					

[A] The Gibbs energy and enthalpy values are given in kJ/mol.
[B] Estimated based on the relationship $\Delta g_{MS}^{\neq}(T_{ref}) = 1.2\Delta g_s^{\neq}(T_{ref}) + 25.38$.

by about 200 mV to 250 mV at 85°C. This phenomenon results from the acceleration of anodic dissolution in the localized environment by the presence of H_2S, which increases the tendency of the alloy to undergo localized corrosion at all chloride concentrations.

In contrast to the 100% H_2S conditions, the effect of H_2S at low concentrations (i.e., 1% H_2S for S13Cr SS, S15Cr SS, and DSS 2507) strongly depends on the chloride concentration and on the particular alloy. At high chloride concentrations, there is little difference between the trends of the curves for 0% and 1% H_2S. As discussed previously,[22] the E_{rp} of S13Cr SS in the presence of 1% H_2S does not decrease below its level in H_2S-free solutions but significantly increases provided that the chloride concentration is sufficiently low. This inhibitive effect is a result of the formation of solid metal sulfide in competition with metal oxide. The net behavior of the system is a result of the competition between the acceleration of anodic dissolution resulting from the adsorption of H_2S and the inhibition resulting from the formation of a protective solid sulfide phase. Because the accelerating effect is promoted by the presence of chlorides, the effect of metal sulfide formation becomes predominant at chloride activities below ca. 0.3 and leads to an increase in the E_{rp} up to 300 mV. It is noteworthy that the inhibitive effect of H_2S at low chloride concentrations is pronounced only for the least CRAs, i.e., for S13Cr SS and S15Cr SS. The inhibition effect is slightly less pronounced for S15Cr SS, for which the E_{rp} increase starts at chloride activities below ~0.1. For DSS 2507, only a very weak inhibition effect is observed at much lower chloride activities, i.e., at ~0.001 compared to ~0.1 for S13Cr SS. This effect can be expected to be related to the Cr content of the alloy (25.17% for DSS 2507 vs. 12.1% for S13Cr SS). A higher Cr content stabilizes the oxide in the repassivation process compared to the sulfide, which is responsible for the H_2S inhibition effect.

As predicted by the model, the behavior of CRAs at intermediate gas-phase H_2S concentrations,

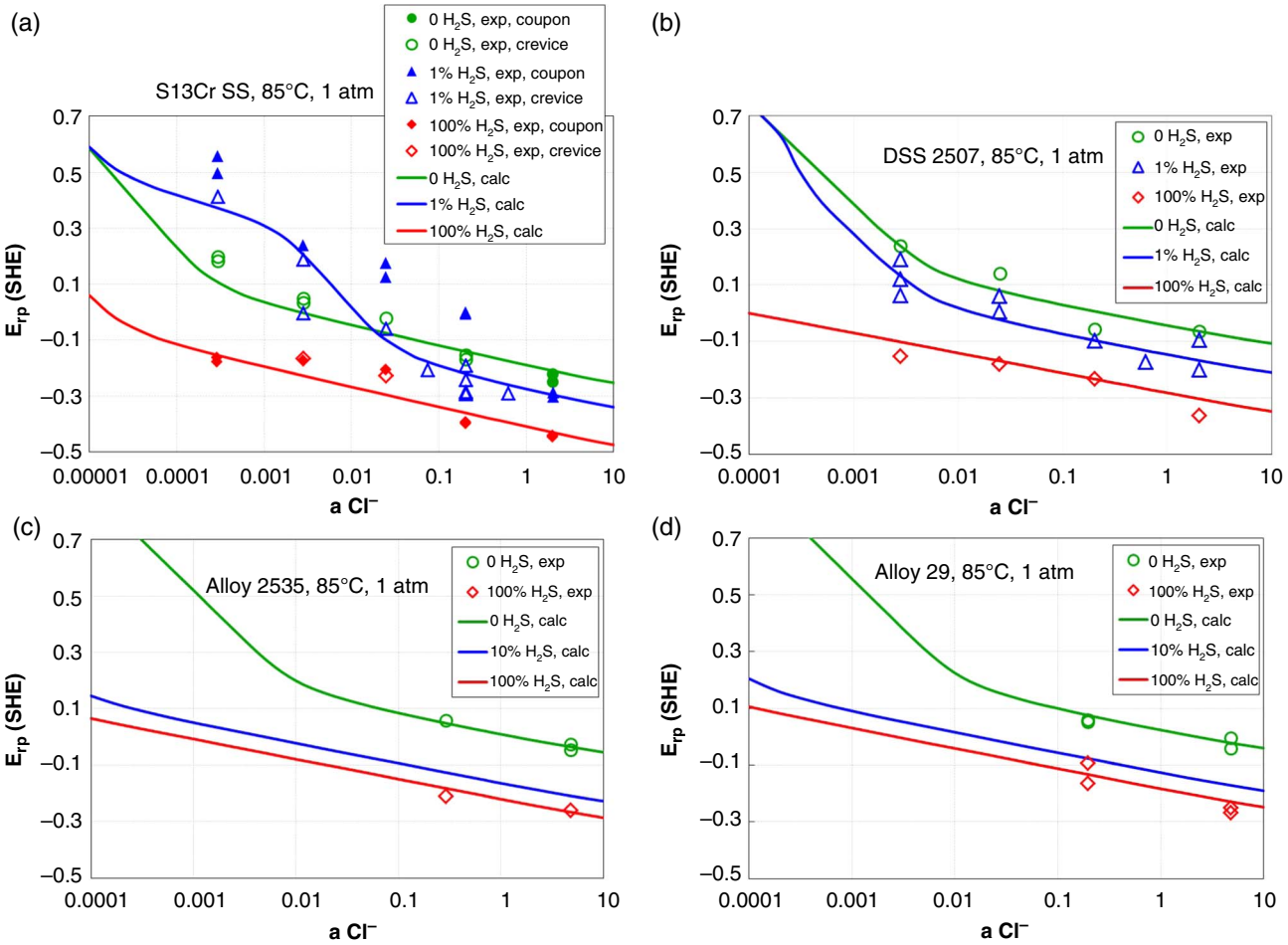

FIGURE 13. *Repassivation potential of (a) S13Cr SS, (b) DSS 2507, (c) Alloy 2535, and (d) Alloy 29 at 85°C in Cl^- + H_2S systems as a function of Cl^- activity at various concentrations of H_2S in the gas phase (0, 1 or 10, and 100 wt%) at room temperature. The lines were obtained from the E_{rp} model.*

i.e., 10%, is very similar to that at 100% H_2S (cf. the diagrams for Alloys 2535, 29, and 28 in Figures 13 and 14). This is because of a strong adsorption of H_2S on surfaces with a high nickel content,[40-41] which precedes the H_2S-induced electrochemical reactions. In cases of strong adsorption, there is not much difference between the availability of adsorbed sulfur on the surface at 10% and 100% H_2S.

Effect of Temperature

The results of E_{rp} calculations for Alloys 2535 and 29 at higher temperatures (232°C and 200°C, respectively) are shown in Figure 15. The red lines for high H_2S concentrations are still largely parallel to the green lines in the absence of H_2S. In contrast to the results at 85°C, the reduction in E_{rp} by the presence of H_2S (75% and 71% H_2S) becomes less pronounced at high temperatures, i.e., it amounts to less than about 100 mV at all chloride concentrations. This indicates that, while an increase in temperature generally increases the tendency for localized corrosion, the relative importance of the presence of H_2S diminishes with temperature.

Effects of Alloying Elements

It is of interest to compare the E_{rp} of the investigated CRAs to understand their relative resistance to localized corrosion. A comparison of six CRAs in H_2S-free environments (solid lines) and in the presence of 100% H_2S in the gas phase (dash/dot lines) at 85°C is shown in Figure 16(a). In the absence of H_2S, E_{rp} increases in the following order (their PRE_Ns are indicated in the parentheses):

$$\text{S13Cr}\,(18) < \text{S15Cr}\,(21) << 28\,(39) < 2507\,(42) < 2535\,(34) < 29\,(42)$$

As expected, the E_{rp} of S13Cr SS and S15Cr SS are significantly lower because of their much lower Cr content. The E_{rp} values for alloys 2507, 2535, 29, and 28 are fairly similar owing to their relatively close Cr and Mo contents. This is in agreement with the relationship between E_{rp} and alloy composition, which has been studied previously.[34] However, the sequence is not quite aligned with their PRE_Ns defined in ISO 15156 – part 3. In particular, the lower E_{rp} value for

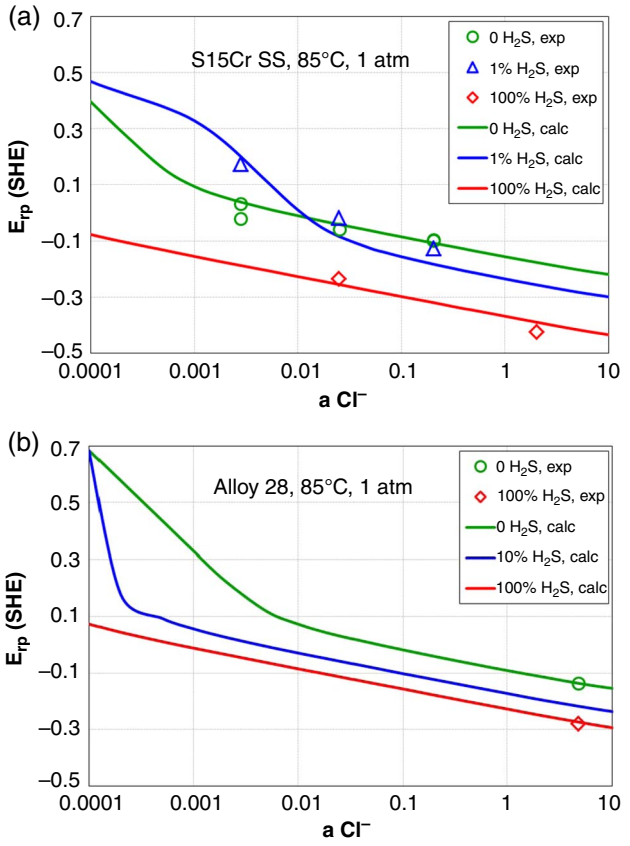

FIGURE 14. *Repassivation potential of (a) S15Cr SS and (b) Alloy 28 at 85°C in Cl^- + H_2S systems as a function of Cl^- activity at various concentrations of H_2S in the gas phase (0, 1 or 10, and 100 wt%) at room temperature. The lines were obtained from the E_{rp} model by using parameters generated for other alloys.*

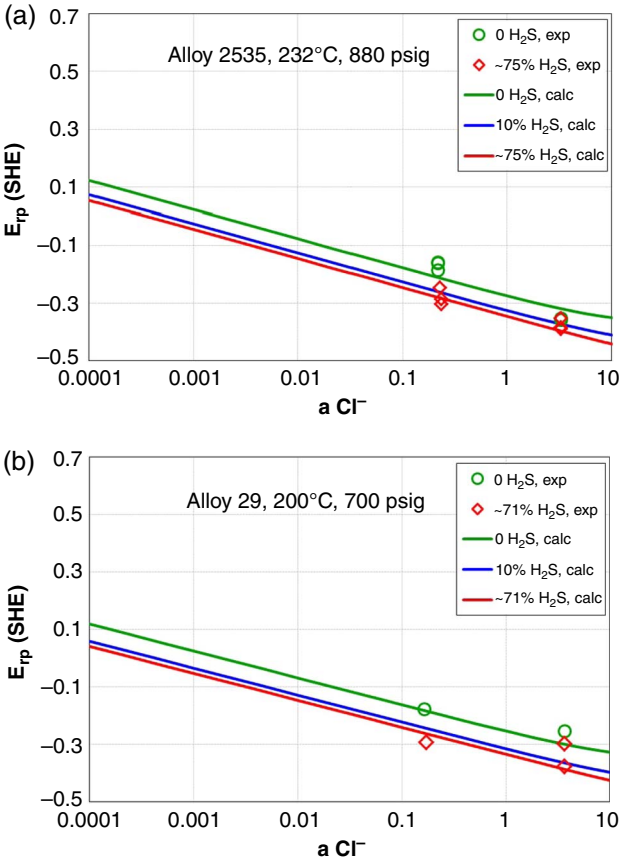

FIGURE 15. *Repassivation potential of (a) Alloy 2535 at 232°C and (b) Alloy 29 at 200°C in Cl^- + H_2S systems as a function of Cl^- activity at various concentrations of H_2S in the gas phase (0, 10, and 75 or 71 wt%) at room temperature. The lines were obtained from the model.*

Alloy 28 than for Alloy 2535 cannot be explained by alloy composition, and hence PRE_N, alone. However, it should be considered that PRE_N is a qualitative measure of localized corrosion resistance, which corresponds closely to the comparison of E_{corr} and E_{rp} rather than E_{rp} alone.

In the presence of 100% H_2S, E_{rp} increases in the order:

$$S13Cr < S15Cr << 2507 < 28 \approx 2535 < 29$$

In this case, E_{rp} of the three Ni-based alloys are very close, which is reflected by similar values of the parameters for the H_2S-accelarated anodic dissolution (i.e., $\Delta g_{ss}^{\neq}(T_{ref})$) in Table 4. Also, the E_{rp} curve for DSS 2507 lies approximately half-way between those for the two martensitic stainless steels and the three Ni-based alloys, whereas it is much closer to the Ni-based alloys in the absence of H_2S. This indicates that E_{rp} in the presence of H_2S is correlated not only with the Cr and Mo content. It is possible that Ni content also plays a significant role the H_2S-containing environments, which may be related to the strong adsorption effect of H_2S on Ni[40-41] and the experimentally observed importance of NiS formation on Fe-Ni-Cr alloys.[43-44]

A comparison of the six CRAs in H_2S-free environments (solid lines) and in the presence of 71% H_2S (dash/dot lines) at 200°C is shown in Figure 16(b). In the absence of H_2S, E_{rp} increases in the order:

$$S13Cr < S15Cr < 2507 \approx 28 < 29 < 2535$$

Because of the significant contribution of Ni content to high-temperature performance, the sequence is roughly aligned with the Ni concentration. Again, as a result of their low Cr content, the two martensitic stainless steels are considerably lower than the other four alloys. However, the differences in the E_{rp} values diminish at 200°C. In the presence of 71% H_2S, E_{rp} increases in the order:

$$S13Cr < S15Cr < 2507 < 28 \approx 2535 < 29$$

At the high H_2S conditions, the E_{rp} lines for three Ni-based alloys are almost indistinguishable and significantly higher than those for the two martensitic stainless steels. DSS 2507 performs closer to the

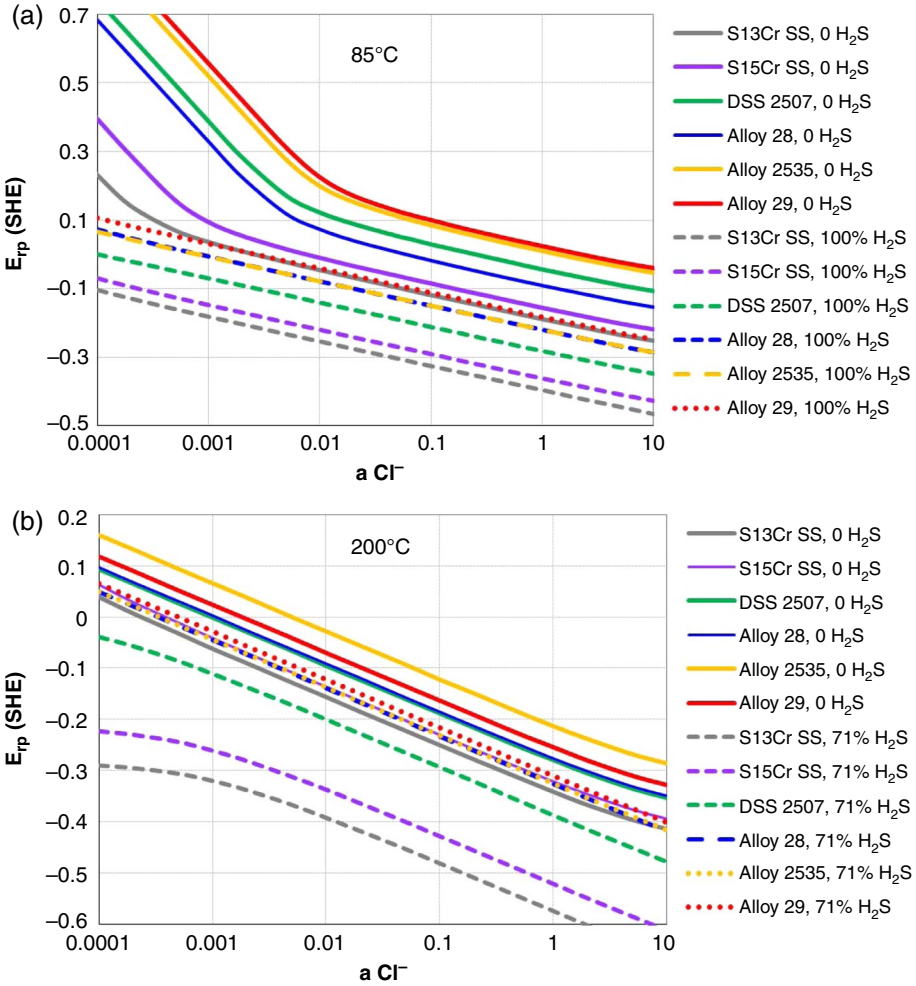

FIGURE 16. *Comparison of calculated repassivation potentials of alloys S13Cr, S15Cr, 2507, 2535, 29, and 28: (a) in the absence of H_2S and in the presence of 100% H_2S in the gas phase at 85°C, and (b) in the absence of H_2S and in the presence of 71% H_2S (defined at room temperature) in the gas phase at 200°C.*

Ni-based alloys at elevated temperature but has somewhat lower E_{rp} values.

CONCLUSIONS

❖ Repassivation potentials have been systematically measured for the corrosion resistant alloys 2507, 2535, and 29 in chloride-H_2S systems at different temperatures. Also, measurements have been made at selected conditions for S15Cr SS and Alloy 28. The repassivation potential represents the tendency of an alloy to undergo localized corrosion and stress corrosion cracking in a given environment.

❖ Absolute oxygen-free environment and stable growth of localized corrosion are critical to determine trustworthy and conservative repassivation potentials for corrosion resistant alloys in H_2S-containing environments.

❖ In most cases, PD-PS-PD and THE are robust methods to measure repassivation potentials of corrosion resistant alloys, which are frequently defined at an inflection point of the reverse scan. However, it is still challenging to identify the onset of localized corrosion and the repassivation process when H_2S oxidation is predominant.

❖ Supported by experimental data, a mechanistic model has been developed and validated to compute the repassivation potential of corrosion resistant alloys as a function of solution chemistry (i.e., concentrations of chloride and H_2S) and temperature. It accounts for competitive adsorption and formation of aggressive/passivating species on the metal surface. Based on limited experimental data, the model is capable of generalizing the experimental database and extrapolating to a wide range of field conditions.

❖ At most conditions, the presence of H_2S substantially reduces the repassivation potential, which indicates enhanced susceptibility to localized corrosion. However, exceptions exist for super-martensitic stainless steels at low H_2S and chloride concentrations.

❖ Elevated temperature diminishes the effect of H_2S on the reduction of the repassivation potential when compared to H_2S-free conditions.
❖ Other than Cr and Mo, Ni content also plays a significant role in increasing repassivation potentials in the presence of H_2S, especially at elevated temperatures.

ACKNOWLEDGMENTS

The work reported here was supported by Chevron, ConocoPhillips, Petrobras, DNV GL, JFE, Nippon Steel & Sumitomo Metal Corp, Sandvik, and Vallourec-Manesmann within the framework of the joint industry program "Performance Assessment of CRAs in Severe Well Environments."

REFERENCES

1. J.M. Bell, Y.D. Chin, S. Hanrahan, "State-of-the-Art of Ultra Deepwater Production Technologies," Offshore Technology Conference (Richardson, TX: Society of Petroleum Engineers, 2005).
2. A. Asphahani, J. Prouheze, G. Petersen, "Corrosion-Resistant Alloys for Hot, Deep Sour Wells: Properties, Experience, and Future Trends," Offshore Technology Conference (Richardson, TX: Society of Petroleum Engineers, 1989).
3. K. Morsi, "Field Experience with Production of Deep Sour Gas Reservoir," SPE Gas Technology Symposium (Richardson, TX: Society of Petroleum Engineers, 1989).
4. S. Wilhelm, R. Kane, *J. Petrol. Technol.* 38 (1986): p. 1051-1061.
5. "Use of Corrosion-Resistant Alloys in Oilfield Environments," (NACE International, Technical Committee Report 1F192, rev. 2000.
6. P.R. Rhodes, *Corrosion* 57 (2001): p. 923-966.
7. "A Working Party Report on Corrosion Resistant Alloys for Oil and Gas Production: Guidance on General Requirements and Test Methods for H_2S Service," The Institute of Materials, European Federation of Corrosion Publications no. 17, 2002.
8. J. Smith, D. Jensen, B. Meyer, *J. Chem. Eng. Data* 15 (1970): p. 144-146.
9. L. Smith, B.D. Craig, "Practical Corrosion Control Measures for Elemental Sulfur Containing Environments," CORROSION 2005, paper no. 646 (Houston, TX: NACE, 2005).
10. NACE TM0177-2005, "Laboratory Testing of Metals for Resistance to Sulfide Stress Cracking and Stress Corrosion Cracking in H_2S Environments" (Houston, TX: NACE, 2005).
11. M. Hay, *Corrosion* 57 (2001): p. 236-252.
12. ISO 15156-2/NACE MR0175, "Petroleum and Natural Gas Industries - Materials for Use in H_2S-Containing Environments in Oil and Gas Production - Part 2: Cracking-Resistant Carbon and Low-Alloy Steels, and the Use of Cast Irons" (Houston, TX: NACE, 2009).
13. ISO 15156-3/NACE MR0175, "Petroleum and Natural Gas Industries - Materials for Use in H_2S-Containing Environments in Oil and Gas Production - Part 3: Cracking-Resistant CRAs (Corrosion-Resistant Alloys) and Other Alloys" (Houston, TX: NACE, 2009).
14. A. Miyasaka, K. Denpo, H. Ogawa, *Corrosion* 45 (1989): p. 771-780.
15. S. Tsujikawa, A. Miyasaka, M. Ueda, S. Ando, T. Shibata, T. Haruna, M. Katahira, Y. Yamane, T. Aoki, T. Yamada, *Corrosion* 49 (1993): p. 409-419.
16. G.A. Cragnolino, D.S. Dunn, N. Sridhar, *Corrosion* 52 (1996): p. 194.
17. G.A. Cragnolino, D.S. Dunn, Y.-M. Pan, N. Sridhar, "The Critical Potential for the Stress Corrosion Cracking of Fe-Ni-Cr Alloys and Its Mechanistic Implications," Chemistry and Electrochemistry of Corrosion and Stress Corrosion Cracking: A Symposium Honoring the Contributions of R.W. Staehle, TMS Annual Meeting 2001 (Warrendale, PA: TMS, 2001), p. 83-104.
18. K. Denpo, H. Ogawa, *Corrosion* 47 (1991): p. 592-597.
19. G. Hinds, L. Wickstroem, J. Abda, A. Turnbull, V. Smith, R. Woollam, *Corros. Sci.* 85 (2014): p. 33-41.
20. A. Anderko, N. Sridhar, D.S. Dunn, *Corros. Sci.* 46 (2004): p. 1583-1612.
21. A. Anderko, N. Sridhar, L.T. Yang, S.L. Grise, B.J. Saidanha, M.H. Dorsey, *Corros. Eng. Sci. Technol.* 40 (2005): p. 33-42.
22. A. Anderko, F. Gui, L. Cao, N. Sridhar, G.R. Engelhardt, *Corrosion* 71 (2015): p. 1197-1212.
23. ASTM G192, "Standard Test Method for Determining the Crevice Repassivation Potential of Corrosion-Resistant Alloys Using a Potentiodynamic-Galvanostatic-Potentiostatic Technique" (West Conshohocken, PA: ASTM International, 2014).
24. ASTM G5, "Standard Reference Test Method for Making Potentiodynamic Anodic Polarization Measurements" (West Conshohocken, PA: ASTM International, 2014).
25. R.W. Bosch, W.F. Bogaerts, J.H. Zheng, *Corrosion* 59 (2003): p. 162-171.
26. D.D. Macdonald, A.C. Scott, P. Wentrcek, *J. Electrochem. Soc.* 126 (1979): p. 908-911.
27. S.H. Oh, C.B. Bahn, W.I. Cho, I.S. Hwang, *J. Electrochem. Soc.* 151 (2004): p. E327-E334.
28. ASTM G61, "Standard Test Method for Conducting Cyclic Potentiodynamic Polarization Measurements for Localized Corrosion Susceptibility of Iron-, Nickel-, or Cobalt-Based Alloys" (West Conshohocken, PA: ASTM International, 2014).
29. D.S. Dunn, G.A. Cragnolino, N. Sridhar, *Corrosion* 56 (2000): p. 90-104.
30. R.M. Carranza, C.M. Giordano, M.A. Rodríguez, R.B. Rebak, "Electrochemical Methods for Repassivation Potential Measurements," CORROSION 2009, paper no. 427 (Houston, TX: NACE, 2009).
31. C.M. Giordano, M.R. Ortiz, M.A. Rodriguez, R.M. Carranza, R.B. Rebak, *Corros. Eng. Sci. Technol.* 46 (2011): p. 129-133.
32. X. He, B. Brettmann, H. Jung, *Corrosion* 65 (2009): p. 449-460.
33. M.R. Ortiz, M.A. Rodriguez, R.M. Carranza, R.B. Rebak, *Corrosion* 66 (2010): p. 105002-1 to 105002-12.
34. A. Anderko, N. Sridhar, M.A. Jakab, G. Tormoen, *Corros. Sci.* 50 (2008): p. 3629-3647.
35. J.F. Zemaitis Jr., D.M. Clark, M. Rafal, N.C. Scrivner, *Handbook of Aqueous Electrolyte Thermodynamics* (New York, NY: John Wiley & Sons, Inc., 1986).
36. M. Rafal, J.W. Berthold, N.C. Scrivner, S.L. Grise, *Models for Electrolyte Solutions*, in *Models for Thermodynamic and Phase Equilibria Calculations*, ed. S.I. Sandler (New York, NY: Marcel Dekker, 1995).
37. A. Anderko, G.R. Engelhardt, F. Gui, L. Cao, N. Sridhar, "Localized Corrosion of Corrosion-Resistant Alloys in Environments Containing Hydrogen Sulfide," CORROSION 2015, paper no. 5562 (Houston, TX: NACE, 2015).
38. J. Enerhaug, U. Steinsmo, Ø. Grong, "Dissolution and Repassivation Kinetics of a 12.3Cr-2.6Mo-6.5Ni Super Martensitic Stainless Steel: A Study of the Effect of H_2S," CORROSION 2007, paper no. 095 (Houston, TX: NACE, 2007).
39. H.Y. Ha, M.H. Jang, T.H. Lee, J. Moon, *Mater. Characterization* 106 (2015): p. 338-345.
40. P. Marecot, E. Paraiso, J.M. Dumas, J. Barbier, *Appl. Catalysis A: General* 80 (1992): p. 89-97.
41. Y. Zhou, J.M. White, *Surf. Sci.* 183 (1987): p. 363-376.
42. M. Ueda, *Corrosion* 62 (2006): p. 856-867.
43. S. Azuma, T. Kudo, *Corrosion* 47 (1991): p. 458-463.
44. P. Marcus, I. Olefjord, J. Oudar, *Corros. Sci.* 24 (1984): p. 269-278.